EUV spectroscopy on NSTX

2010 J. Phys. B: At. Mol. Opt. Phys. 43 144018

(http://iopscience.iop.org/0953-4075/43/14/144018)

J. Phys. B: At. Mol. Opt. Phys. **43** (2010) 144018 (10pp) doi:10.1088/0953-4075/43/14/144018

EUV spectroscopy on NSTX

J K Lepson[1], P Beiersdorfer[2], J Clementson[2], M F Gu[1], M Bitter[3], L Roquemore[3], R Kaita[3], P G Cox[4] and A S Safronova[4]

[1] Space Sciences Laboratory, Berkeley, CA 94720, USA
[2] Lawrence Livermore National Laboratory, Livermore, CA 94550, USA
[3] Princeton Plasma Physics Laboratory, Princeton, NJ, USA
[4] University of Nevada, Reno, NV 89557, USA

E-mail: lepson@ssl.berkeley.edu

Received 7 December 2009, in final form 16 February 2010
Published 5 July 2010
Online at stacks.iop.org/JPhysB/43/144018

Abstract
Spectroscopy in the extreme ultraviolet region is important to magnetic fusion research as well as to astrophysics. We report on XEUS (X-ray and Extreme Ultraviolet Spectrometer) and LoWEUS (Long-Wavelength and Extreme Ultraviolet Spectrometer), which operate in the 5–400 Å region on the NSTX (National Spherical Tokamak Experiment) tokamak. The instruments are being used to survey impurities, both for intrinsic elements present in the plasma and for metal impurities resulting from damage to various components. In addition, we have used XEUS and LoWEUS to investigate density-dependent and temperature-dependent emission lines for diagnostic use.

(Some figures in this article are in colour only in the electronic version)

1. Introduction

Spectroscopy is an essential tool for plasma diagnostics, both of laboratory and astrophysical plasmas. In magnetic fusion research, spectroscopy provides a record of impurities present in the plasma, and it provides a determination of electron temperature and density, ion temperature and bulk ion velocity. The paper by Stratton *et al* (2008) gives a recent in-depth review of spectral diagnostics for magnetic fusion.

Extreme ultraviolet (EUV) spectroscopy has played an especially important role in plasma diagnostics. For example, EUV spectroscopy on the Princeton Large Torus in the 1970s revealed problems caused by high-Z impurities in the plasma core (Hinnov *et al* 1978). It was found that high-Z impurities could radiate half of the input power, thereby severely reducing the central plasma temperature. These findings led to new tokamak designs and techniques.

EUV spectroscopy is an excellent tool as an impurity monitor because of the abundance of emission lines from many elements in this region. This is true for fusion devices and for astrophysical plasmas. EUV spectroscopy has been an important part of such observing missions as the Extreme Ultraviolet Explorer, the Chandra X-ray Observatory and the Hinode solar satellite. On Earth, a number of instruments have been designed and implemented as impurity monitors for fusion plasma devices, for example, SOXMOS (Schwob *et al* 1987), which is currently used on the Large Helical Device (Kato *et al* 2008), and SPRED (Fonck *et al* 1982), which is used on the National Spherical Tokamak Experiment. More recently, the EUV_Short and EUV_Long spectrometers have been developed and installed on LHD (Chowdhuri 2008a, 2008b).

In 2004, we installed a high-resolution grating spectrometer on NSTX (Beiersdorfer *et al* 2006), which was later dubbed XEUS, the X-ray and Extreme Ultraviolet Spectrometer. This spectrometer had been previously used for laboratory astrophysics measurements at the Lawrence Livermore electron beam ion trap (EBIT) facility (Beiersdorfer 2003, Lepson *et al* 2008), and has an ∼50 Å field of view that can be positioned to cover the region from 5 to 135 Å. The XEUS is one of a series of instruments that were developed at the Livermore EBIT facility and then moved to magnetic fusion energy devices (Beiersdorfer *et al* 2004, Clementson *et al* 2008, Graf *et al* 2008). Another grating spectrometer, added to NSTX in 2008, is LoWEUS, the Long Wavelength and Extreme Ultraviolet Spectrometer, which covers the region from 60 to 400 Å with an ∼160 Å field of view (Beiersdorfer *et al* 2008).

The installation of XEUS and LoWEUS on NSTX has provided a new look at the EUV emission because the resulting spectra have a much higher resolution than that of typical SPRED survey spectra. This is important for a number

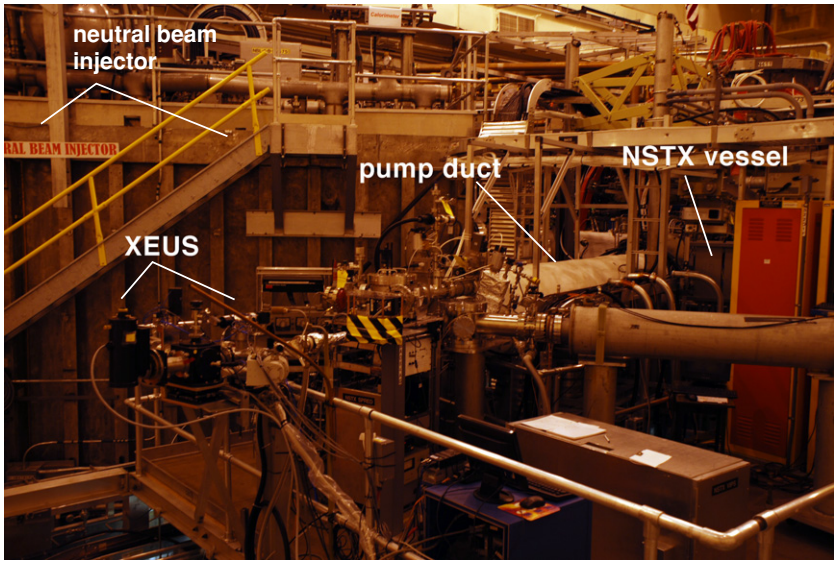

Figure 1. XEUS setup on NSTX.

of reasons. First, to determine the intensity (amount) of impurities. Second, to determine under what conditions impurities occur, such as during radio frequency heating or lithium injection to suppress edge-localized modes (ELMs). Does the plasma contact the components and do certain conditions cause ablation of metal components? Third, with the recent addition of new cameras and software, we are now able to study the time dependence of the plasma emission and resolve when the impurities arise, which can also help determine their source. Fourth, because it extends to a much shorter wavelength region than most other grating instruments, XEUS has been able to monitor such features as the L-shell emission of argon, iron, nickel and copper. Finally, going beyond the needed surveys of plasma impurity monitoring, XEUS and LoWEUS have enabled new experiments, for example, with neon and tungsten in transport studies to determine if the material can penetrate the core and if so, how far into it (Delgado-Aparicio *et al* 2009, Clementson *et al*, in preparation), and the calibration of density diagnostics of argon and iron for astrophysics (Lepson *et al* 2008).

In this paper, we will present spectral surveys of NSTX carried out with XEUS and LoWEUS showing lithium, boron, carbon, nitrogen, oxygen, neon, titanium, iron, nickel, copper and molybdenum lines, as well as density-dependent lines of iron and argon, which can be compared to spectra from lower density EBIT plasmas.

2. Spectroscopic instrumentation on NSTX

As already mentioned, XEUS and LoWEUS were both developed at the Livermore EBIT facility for use in laboratory astrophysics. XEUS was added to NSTX in 2004, where it was installed at the end of the pump duct next to the neutral beam injector, as shown in figure 1. LoWEUS was installed below the RF antennae on NSTX in 2007, as shown in figure 2.

XEUS (pronounced 'Zeus') is a grazing incidence spectrometer utilizing a varied-line-space flat-field spectrometer

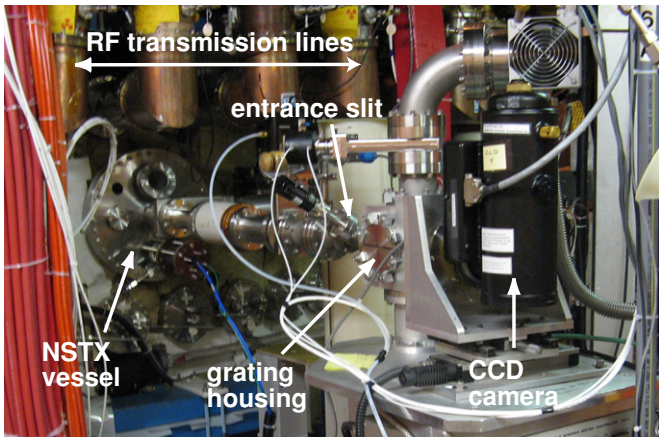

Figure 2. LoWEUS setup on NSTX.

flat-field grating originally developed by Harada and Kita (1980) and Nakano *et al* (1984). It has an average spacing of 2400 ℓ mm^{-1} and operates at a 1.3° angle of incidence (Utter *et al* 1999). XEUS has a field of view of ~50 Å and can be positioned to survey between 5 and 135 Å with an instrumental resolution of ~0.1 Å and $\lambda/\Delta\lambda \sim 100$ at 10 Å to 1000 at 100 Å.

LoWEUS (pronounced 'Lois') is similar to XEUS, but it is equipped with a grating with an average spacing of 1200 ℓ mm^{-1} and an operating angle of 3° (Beiersdorfer *et al* 1999). It has a field of view of ~180 Å and can be positioned to monitor emission between ~60 Åand 400 Å. LoWEUS has an instrumental resolution $\lambda/\Delta\lambda \sim 300$ at 100 Å to 600 at 200 Å.

Readouts from both instruments are taken with a back-illuminated, liquid nitrogen-cooled CCD camera with an approximately 1 inch square array of 1300 × 1340 pixels. Both instruments utilize either 30 μm or 100 μm entrance slits.

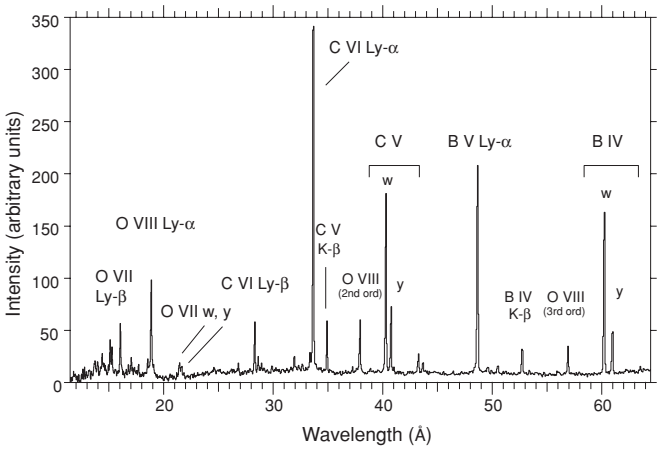

Figure 3. Emission lines of oxygen, carbon and boron as seen by XEUS. Kβ refers to the $1s3p\,{}^1P_1 \rightarrow 1s^2\,{}^1S_0$ transition in helium-like ions.

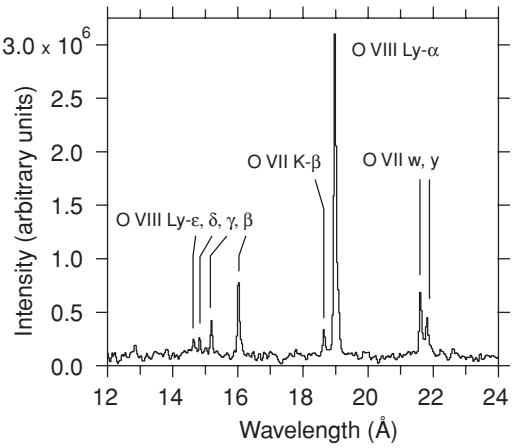

Figure 4. Expanded view of the emission lines of helium-like O VII and hydrogen-like O VIII.

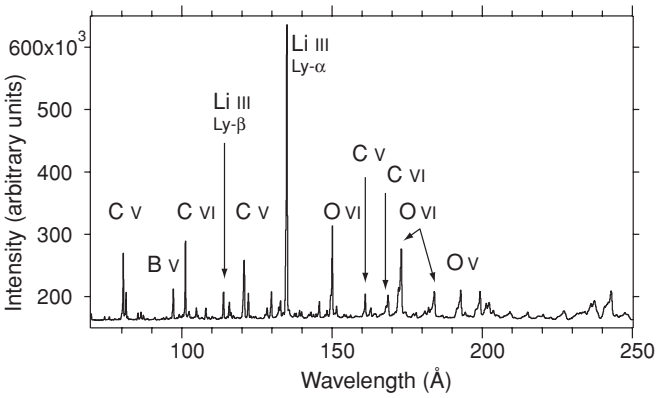

Figure 5. Emission lines of oxygen, carbon and lithium as seen by LoWEUS. Lines of carbon and boron are higher order reflections of those seen in figure 3.

Wavelength calibrations are performed by using the well-known K-shell emission lines of hydrogen-like and helium-like ions commonly known as Lyman-α and w, respectively, depending on which lines fall into a given spectral range, i.e. lithium, boron, carbon, nitrogen or oxygen. Some of these lines are observed in higher orders and thus provide additional calibration benchmarks. In addition, after an initial wavelength scale is established with the help of the aforementioned K-shell lines, we further anchor the calibration by using other well-known lines that appear periodically depending on the plasma conditions, including the 2–2 L-shell emission lines of iron (Fe XVIII–XXIII) and oxygen (O V–VI). This provides an accurately calibrated region from 10–200 Å which has been the most studied region in NSTX.

Because XEUS is installed near the neutral beam injector, it is subject to high doses of hard x-rays during shots with neutral beam heating. Some of the hard x-rays are the result of the high acceleration potential in the neutral beam injector, which can lead to a high x-ray background on the CCD even when there is no plasma. During plasma shots, the hard x-rays cause considerable noise in the image, depending on the neutral beam power. In some shots (see below), spectral lines can be nearly invisible through the beam noise, but in others the emission lines are so intense that they dwarf the beam noise. In 2009, we installed lead shielding which mitigated this problem to some extent. LoWEUS is situated on the far side of the vacuum chamber from the neutral beam injector and is thus nearly unaffected by the hard x-rays that impact XEUS.

3. Surveys of impurities in NSTX plasmas

In this section, we present several spectra from XEUS and LoWEUS to illustrate their use in surveys of impurities in NSTX plasmas.

A typical, 'clean' discharge (i.e. without metal impurities) recorded by XEUS is shown in figure 3, which illustrates the time-integrated emission from shot 118080. The spectrum is dominated by the hydrogen-like and helium-like emission of O VII and VIII, C V and VI, and B IV and V that are used for calibration as mentioned in the previous section. The strongest feature is typically the Lyman-α line (an unresolved blend of the $2p_{3/2} \rightarrow 1s_{1/2}$ and $2p_{1/2} \rightarrow 1s_{1/2}$ transitions) of C VI (from the graphite surface of the vessel wall) at 33.73 Å followed by the Lyman-α lines of B V at 48.58 Å and O VIII at 18.97 Å. Although boron is typically weaker than oxygen, it becomes prominent and sometimes even dominant following boronization. Other lines include the Lyman-β line ($3p_{3/2} \rightarrow 1s_{1/2}$ and $3p_{1/2} \rightarrow 1s_{1/2}$ transitions) of O VIII, C VI, and B V, and the w ($1s2p\,{}^1P_1 \rightarrow 1s^2\,{}^1S_0$) and y($1s2p\,{}^3P_1 \rightarrow 1s^2\,{}^1S_0$) lines of O VII, C V and B IV. The O VIII Lyman-α line is also visible in second order at 37.94 Å and in third order at 56.91 Å. Nitrogen is only rarely seen in NSTX discharges, which indicates that there are no air leaks and, as a corollary, that the oxygen is from sources other than air.

Figure 4 focuses on the emission of O VII and O VIII. The Lyman series is readily distinguishable down to the Lyman-ϵ line, i.e. the blend of the transitions $6p_{3/2} \rightarrow 1s_{1/2}$ and $6p_{1/2} \rightarrow 1s_{1/2}$.

Figure 5 shows a typical spectrum from LoWEUS. Emission in the region shown is dominated by the Lyman-α

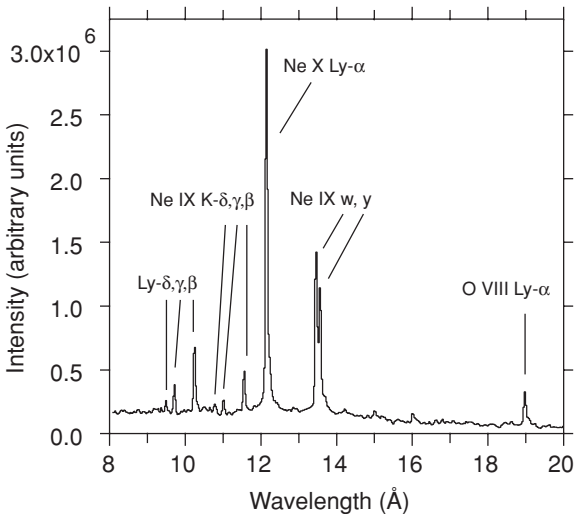

Figure 6. Emission lines of helium-like Ne IX and hydrogenic Ne X after neon puffing into NSTX.

line of Li III at 134.94 Å. The Lyman series of lithium (dropped in as a powder or evaporated via LITER, the LIThium EvaporatoR) is also noticeable. Higher orders of the C V and C VI K-shell lines are seen from 80 to 240 Å, which are used for wavelength calibrations. Because of some difficulties with the camera placement and focusing in 2009, the lines became much broader above 200 Å; this focusing issue has since been resolved.

The spectra from 'clean' NSTX discharges, showing essentially only lines from lithium, boron, carbon and oxygen, can be used as baselines for detecting the influx of other impurities into the plasma. Example impurities seen are neon, argon, titanium, iron, nickel and molybdenum. By detecting these impurities in the EUV spectra, an effort can be made to pinpoint the source of the material, and corrective action—if needed—can be taken, as illustrated in the following.

Figure 6 shows extremely strong emission of Ne X after neon was used for discharge cleaning on NSTX. The Ne X Lyman-α line dwarfs the emission of O VIII and C VI that normally dominates the plasma. The intensity of the neon emission quickly decreased in subsequent shots.

The most commonly seen metal impurity is iron, followed by copper and nickel. Iron, nickel and chromium are present in NSTX as the makeup of stainless steel found in the outer wall and in a number of hardware components, such as detector boxes, brackets, shutters, and shielding on magnetic sensors and cables. Copper, titanium, and molybdenum are found in the RF heating antennae and various shielding, and the neutral beam duct has molybdenum as well. The presence of metals in NSTX plasma is often an indication that the hot plasma is ablating or melting the components, degrading both the instruments and the plasma conditions, and is often associated with edge localized modes (ELMs). Identification of metal impurities provides information on which components are affected and to what degree.

Figure 7 is a spectrum from XEUS that shows a strong emission of Fe XVII and Cu XX between 7 and 20 Å. The emission of iron and copper includes many unresolved lines that 'pile up' into a pseudo-continuum. A detailed comparison between XEUS data and theory of the spectral region between 5 and 17 Å has been presented in Beiersdorfer *et al* (2004). This comparison has shown the presence of L-shell nickel transitions together with those of iron. The presence of copper in this line cluster is new in 2009. A blow-up of the 7–20 Å region is shown in figure 8, where the copper lines are clearly enhanced over those of iron, allowing ready identification of the Cu XX features. The strongest lines in the neon-like emission of copper and iron are labelled in the notation of Beiersdorfer *et al* (1988). Specifically, the lines 3C, 3D, 3F and 3G are electric dipole transitions from upper levels $2p^5_{1/2}3d_{3/2}$, $2p^5_{3/2}3d_{5/2}$, $2p^5_{1/2}3s_{1/2}$ and $2p^5_{3/2}3s_{1/2}$ to the closed shell $2p^6$ ground state, respectively. The line labelled M2, which blends with the line 3G, in the spectrum shown, is a magnetic quadrupole transition from the upper level $2p^5_{3/2}3s_{1/2}$ ($J = 2$). Plasma conditions were very similar for figures 4 and 8 (T_e max 1.25 keV, n_e max 10^{14} cm^{-3}, neutral beam 4 MW), indicating that presence of metal impurities is not easily associated with such parameters as neutral beam heating, electron temperature or electron density.

M-shell emission of iron and nickel is illustrated in figure 9, which includes M-shell emission lines of Ni IX–XIV and Fe VIII–XII. This region is of particular interest to

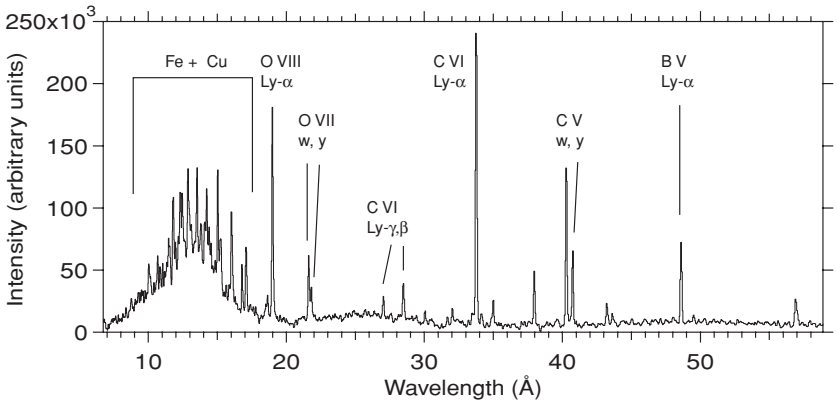

Figure 7. L-shell emission of copper and iron on NSTX.

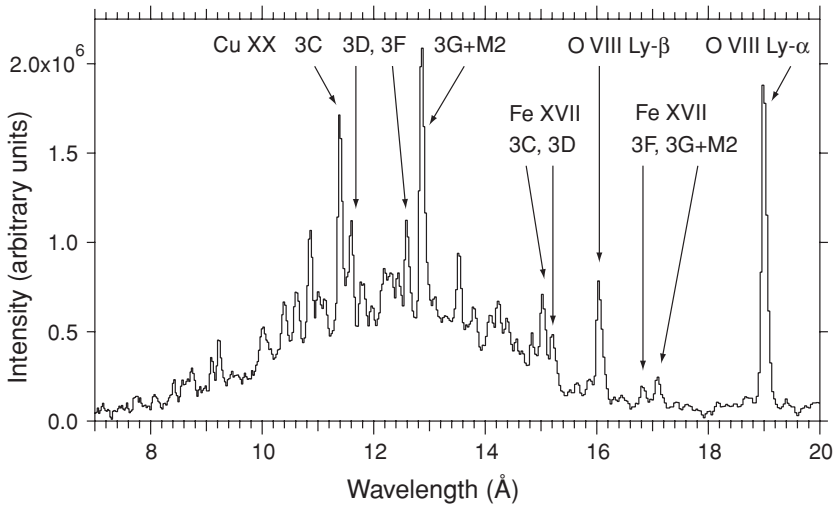

Figure 8. Identification of L-shell emission of copper on NSTX.

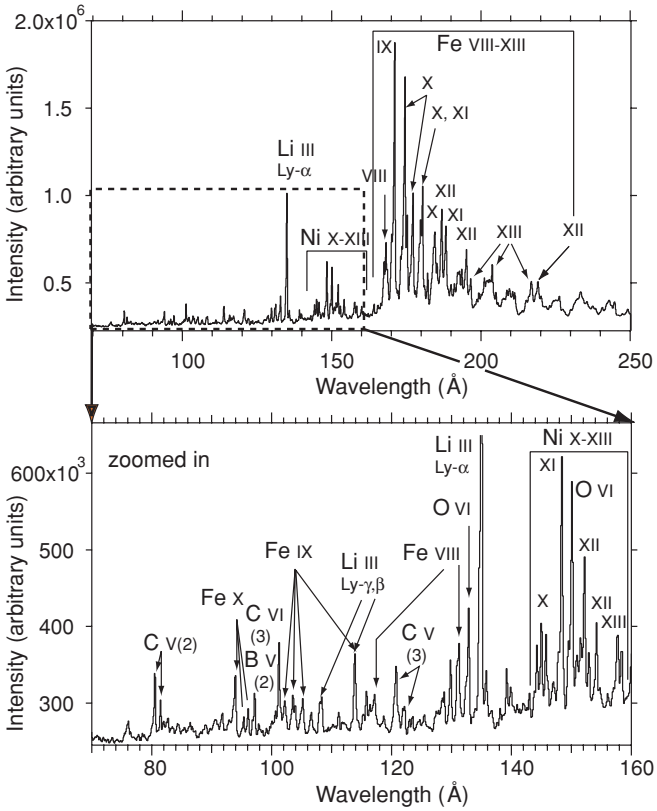

Figure 9. M-shell emission lines of nickel and iron as seen by LoWEUS in NSTX shot 134631.

x-ray astronomers as it contains the widely used Fe IX line at 171.1 Å. It also contains a number of important 2–2 lines of O V and O VI.

Titanium is seen infrequently and only in small amounts. Figure 10 shows the neon-like Ti XIII emission along with the much stronger neon-like Fe XVII features. We have overlaid calculations from the Flexible Atomic Code (Gu 2008) that identify the presence of titanium in this spectrum.

The effect of hard x-rays from the neutral beam injector is apparent in figure 11, which shows lines of molybdenum and iron. Argon-like Mo XXV is seen—barely—at 73.85 Å while Fe XVIII is found at 93.9 Å and Fe XX at 99.2 Å. The lines are almost indistinguishable from the x-ray noise in the spectrum; the fact that the lines can be faintly seen in the 2D original image from the CCD camera (Lepson and Beiersdorfer 2005) indicates that they are real and not 'false peaks' from hard x-rays. Identification of Mo XXV was aided by calculations from the Flexible Atomic Code (Gu 2008).

4. Density diagnostics on NSTX

Many EUV emission lines vary in strength depending on plasma conditions. The effects of temperature are universally and obviously seen in the charge balance as higher temperatures excite more highly ionized ions as electrons are stripped free. Line strengths may also vary due to factors such as plasma density and even magnetic field strength (Beiersdorfer *et al* 2003). In ideal cases, two lines of similar wavelength will vary differently with respect to plasma conditions, such as density, and their ratio can be used as a diagnostic tool. While the effects of collisional excitation or de-excitation can be calculated, laboratory measurements are needed to confirm—and sometimes correct—the predicted line ratios. In this section, we will briefly discuss density-dependent lines of Ar XIV, Ar IX and Fe XXII.

Argon is not normally present in NSTX or its components, but can be introduced for experiments. Here we used XEUS to examine a shot with argon injection and to investigate density-dependent line pairs of Ar XIV and Ar IX. Figure 12 is a spectrum taken with XEUS after argon injection. Lines of Ar IX through Ar XVI are visible in addition to those of the intrinsic carbon and oxygen. The boron-like 2p–3d transition multiplet of Ar XIV at ∼27.5 Å is density dependent, with collisional redistribution among the ground state fine structure levels affecting the strength of the feature at 27.6 Å. Figure 13 shows the line ratio curve calculated by the Flexible Atomic Code along with measurements from NSTX and lower density plasma at the Livermore EBIT facility. The EBIT ratios as a whole show a reasonable match to theory, but have some significant divergence at higher density, while the NSTX ratio

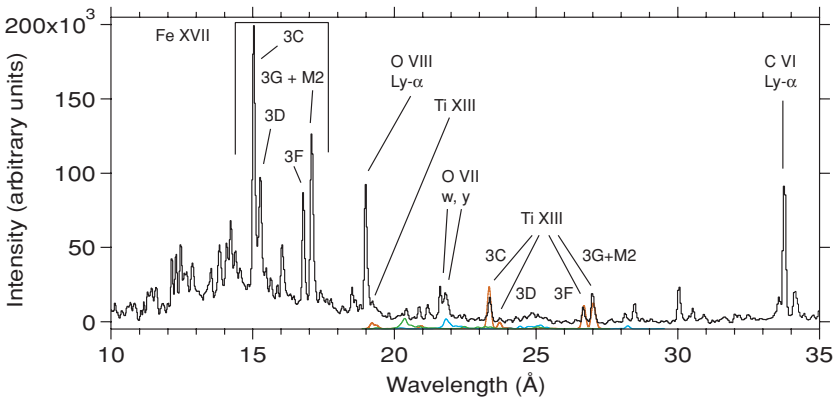

Figure 10. L-shell emission of iron and titanium as seen by XEUS. The spectrum is overlaid with calculations of titanium performed with the Flexible Atomic Code (online: red = Ti XIII, blue = Ti XIV, green = Ti XV).

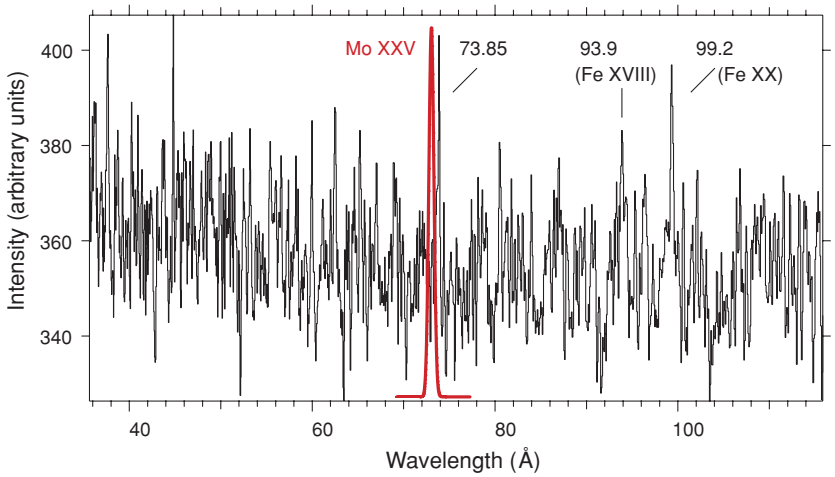

Figure 11. Argon-like Mo XXV, fluorine-like Fe XVIII and nitrogen-like Fe XX as seen by XEUS. Lines are nearly indistinguishable from the hard x-ray noise resulting from neutral beam injector operation. Calculations using the FAC are shown to aid identification of the Mo XXV line.

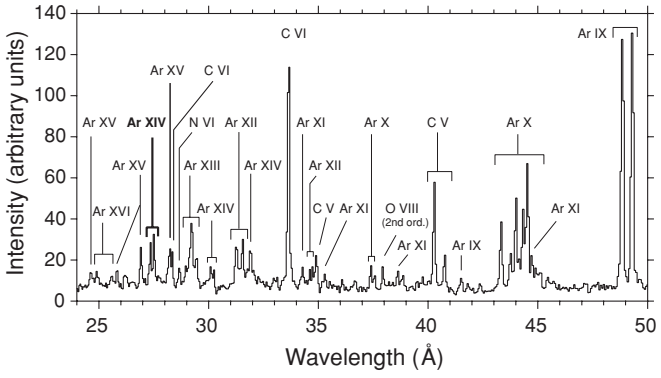

Figure 12. Spectrum taken with XEUS showing argon emission lines on NSTX. The density-dependent boron-like Ar XIV line pair at 27.4 and 27.6 Å is highlighted in bold face.

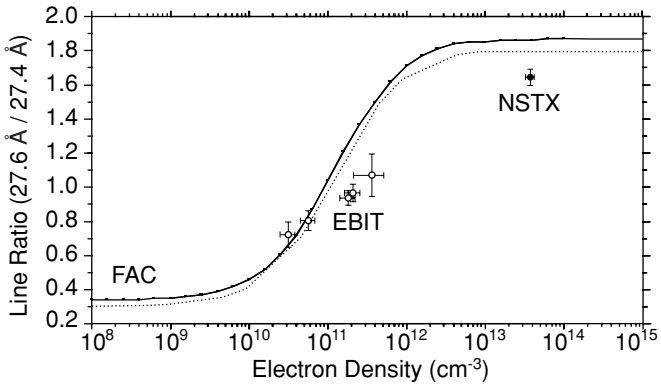

Figure 13. Density-dependent ratios of the boron-like Ar XIV 27.6/27.4 Å line pair (highlighted in bold face in figure 12) as calculated by the Flexible Atomic Code, adapted from Chen *et al* (2004). The solid line is calculated with an electron temperature of 0.3 keV for comparison with NSTX data and the dotted line is calculated with an electron energy of 1.0 keV for comparison with EBIT data. EBIT values are indicated by open circles and the NSTX value by a filled circle.

is substantially smaller than predicted. Together they indicate that the atomic calculations need more work, i.e. theoretical studies will need to be performed to identify the reason for the reduced ratio at high densities.

Density sensitivity also exists in the case of the 3s–2p lines of neon-like Ar IX around 49 Å as seen in figure 14. Here the line M2 is collisionally de-excited and is consequently much weaker in the denser plasma of NSTX than in the low-density electron beam of EBIT-I.

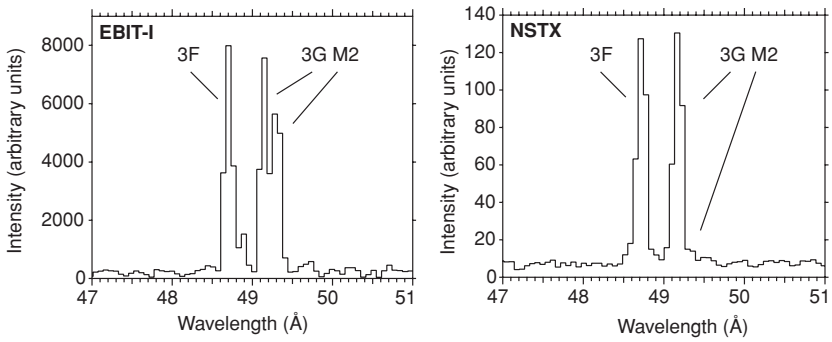

Figure 14. Density-dependent emission lines of neon-like Ar IX. The line labelled M2 is collisionally de-excited and thus diminishes at higher densities. Left: spectrum from the Livermore EBIT-I electron beam ion trap, taken at an electron density of $\sim 5 \times 10^{11}$ cm^{-3}, showing a strong M2 line. Right: spectrum from NSTX, taken at an electron density of $\sim 4 \times 10^{13}$ cm^{-3}, showing only a very weak M2 line.

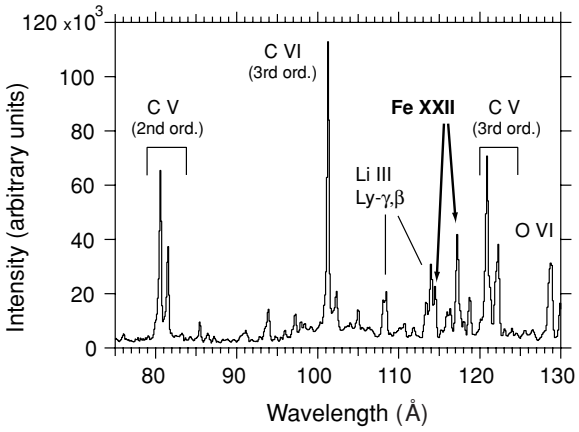

Figure 15. Spectrum taken with LoWEUS (shot 135904) showing density-dependent lines of Fe XXII on NSTX, highlighted in bold face, at 114.4 and 117.1 Å.

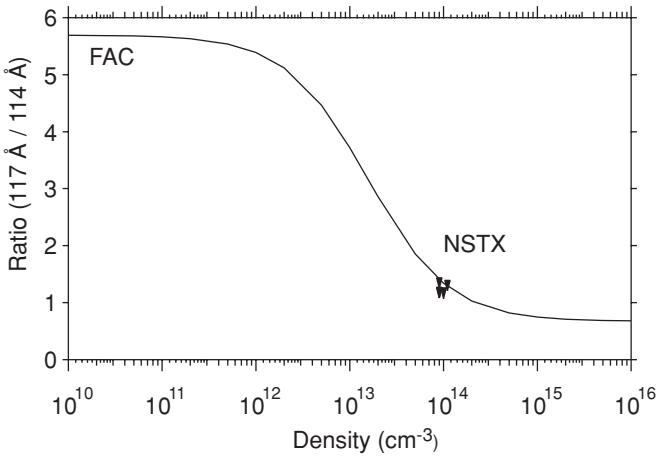

Figure 16. Ratios of the 117/114 Å Fe XXII line pair calculated with the Flexible Atomic Code as a function of electron density. NSTX values are indicated by filled triangles.

In figure 15 we show a spectrum of Fe XXII taken with LoWEUS. Fe XXII has the same electronic configuration as Ar XIV, and the density dependence in this boron-like ion is again caused by the collisional rearrangement of the ground-state fine-structure levels. The main difference to the Ar XIV example we showed above is that we are considering 2–2 transitions in our example of Fe XXII lines instead of 2–3 transitions in Ar XIV. The $1s^2 2s 2p^2\ ^2P_{3/2} \rightarrow 1s^2 2s^2 2p\ ^2P_{3/2}$ line at 117.1 Å decreases relative to the $1s^2 2s 2p^2\ ^2P_{1/2} \rightarrow 1s^2 2s^2 2p\ ^2P_{1/2}$ line at 114.4 Å as plasma density increases. Figure 16 shows the ratio of the two lines between electron densities of 10^{10} and 10^{16} cm^{-3} as calculated with the Flexible Atomic Code (Gu 2008). The ratios measured with LoWEUS on NSTX agree well with theory in this instance.

5. Time-resolved measurements

Time-integrated measurements, as shown in the previous two sections, convey a great deal of information, but studies of the evolution of the plasma over the shot can be important as well. We have recently been able to make time-resolved measurements with XEUS and LoWEUS that provide important information on when various impurities begin to appear and how they change during the shot (Beiersdorfer *et al* 2008). Data shown here are taken with a resolution of ~90–130 ms, but we have more recently achieved a resolution of under 50 ms. Hardware upgrades are currently under way to increase the time resolution by another order of magnitude.

Figure 17 is a shot measured by XEUS with 130 ms time resolution. In this shot, we see that the metal impurities (iron and copper) appear after 390 ms and rapidly gain strength, corresponding to the cessation of the neutral beam source C, which is the strongest (4 MW) of the three neutral beam sources.

Figure 18 shows the evolution of the Lyman-α lines of N VII, C VI and B V in a shot dominated by nitrogen. It is clear that the three elements arise at different times and their relative strengths differ over the period of the shot. At first, carbon is dominant, but it is soon eclipsed by nitrogen and later boron. Although nitrogen is thought to come from insulation made of boron nitride, so that boron and nitrogen should change together, boron continues to increase in strength while carbon and nitrogen are already declining. The ratios thus change during the shot.

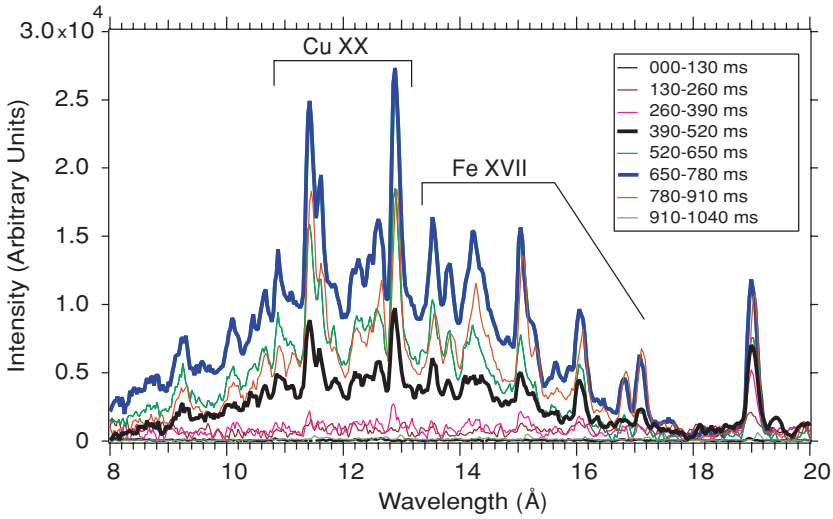

Figure 17. Metal impurities in NSTX plasma seen with XEUS in time-resolved mode. Cu XX and Fe XVII appear after the end of neutral beam source C operation around 390 ms (in thick trace) into the shot. The maximum emission was at 650–780 ms. Each frame covers ∼130 ms.

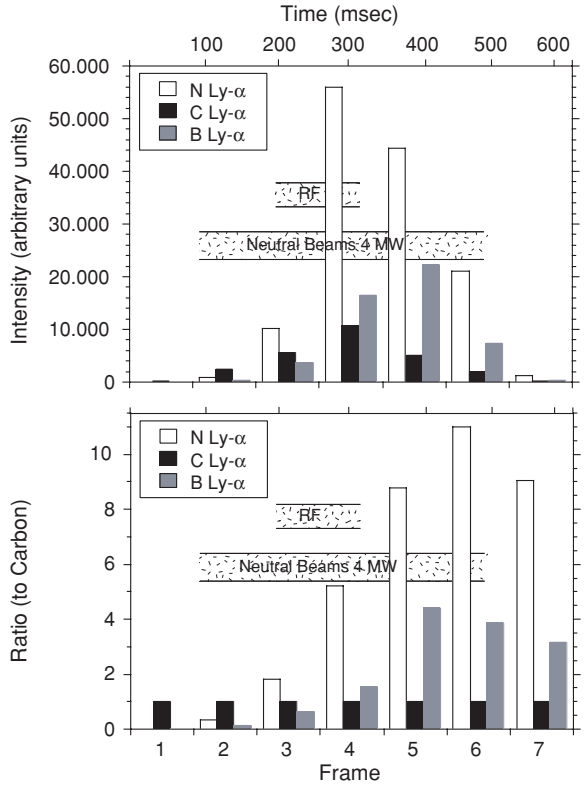

Figure 18. Evolution of three dominant intrinsic impurities in NSTX. Bars show changing intensities of nitrogen, carbon and boron. Each frame covers ∼90 ms. Top: absolute intensities. Bottom: intensities relative to carbon.

6. Electron temperature diagnostics

As we already mentioned, the electron temperature can be inferred from the ionization balance of a given element in the observed spectra. This procedure is widely used in astrophysical and high-density plasmas where non-spectroscopic techniques are not available. On NSTX, the primary electron temperature measurement is provided by Thomson scattering. The electron temperature of NSTX plasmas peaks in the core and tends towards zero near the plasma edge. Because our measurements are not spatially resolved, the ionization balance inferred from the spectrum, therefore, does not represent a local measurement. However, by comparing the inferred abundances of two or three neighbouring ionization states, we can infer a rough effective temperature at which these ions radiate and can test for consistency with the calculations.

Non-LTE kinetic models of O and Li were constructed, at the University of Nevada, Reno (Wilcox *et al* 2008), for comparison with the most diagnostically important features of oxygen and lithium between 100 and 250 Å observed on NSTX. The models include ionization stages with a detailed structure, such as the singly excited states of hydrogen-like ions up to $n = 6$, helium-like ions up to $n = 7$, and doubly excited levels for helium-, lithium- and beryllium-like ions. Energy level structures and complete radiative and collisional coupling data were calculated with the Flexible Atomic Code. We applied the collisional radiative model SCRAM (Hansen 2003) to calculate the EUV spectra of the included low-Z ions.

Theoretical synthetic spectra of oxygen calculated at an electron density of 10^{14} cm^{-3} for two different electron temperatures $T_e = 20$ eV and 100 eV are given in figure 19. The figure shows that at the lower $T_e = 20$ eV, the spectral features of O V make a substantial contribution into the spectrum (average charge $Z_{\rm eff} \sim 4.7$) and vanish as T_e increases up to 100 eV where O VI dominate this part of the spectrum ($Z_{\rm eff} \sim 6.0$).

Figure 20 presents the modelling of the experimental spectrum from NSTX shot 129294 which reveals plasma conditions of relatively low $T_e = 25$ eV for both oxygen and lithium emission. We can correlate the inferred electron temperature to a plasma radius of <30 cm at which the oxygen radiation was produced in NSTX.

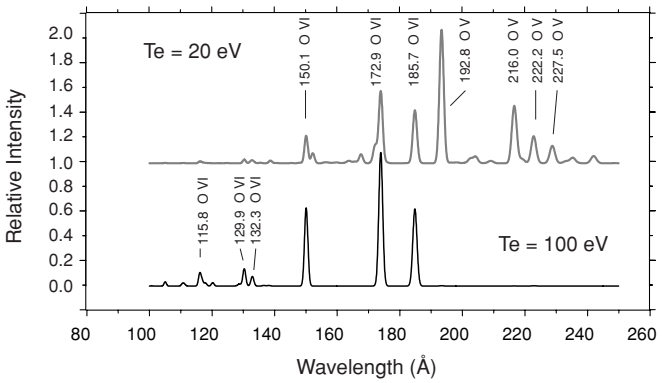

Figure 19. Temperature dependence of theoretical spectra of oxygen calculated at $n_e = 10^{14}$ cm^{-3} for electron temperatures $T_e =$ 20 eV (top) and $T_e = 100$ eV (bottom).

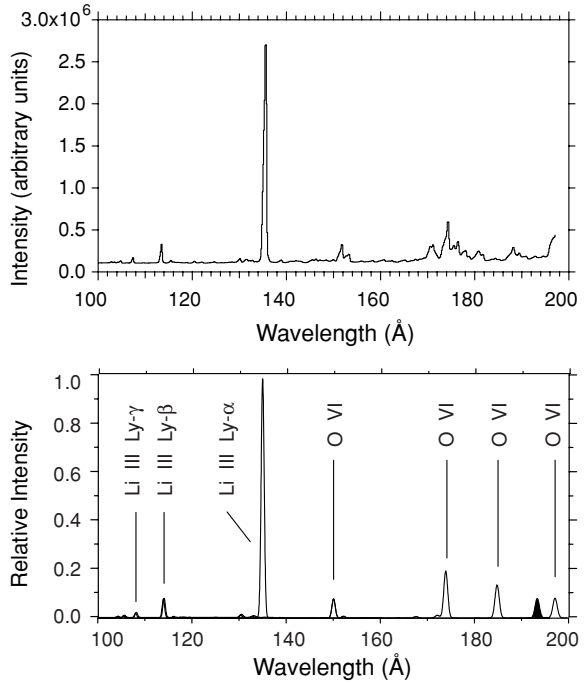

Figure 20. Top: experimental oxygen spectrum taken with LoWEUS (shot 129294). Bottom: theoretical spectrum calculated at $T_e = 25$ eV and $n_e = 10^{14}$ cm^{-3} at the bottom.

7. Conclusion

EUV spectroscopy plays an important role in quantifying the constituents of NSTX plasma and understanding its behaviour. The XEUS and LoWEUS spectrometers, which focus on the wavelength band containing the K-shell lines of lithium through neon and the L-shell lines of nitrogen through copper, are valuable as impurity monitors because of their high resolution, which makes it easier to detect even small quantities of non-standard metal impurities. The recent addition of time resolution has further increased their utility.

The measurements provided by XEUS and LoWEUS are also very useful for testing and improving atomic theory and spectral modelling codes. Improved atomic data are especially important for astronomy, which relies heavily on atomic spectra for inferring the plasma parameters. The iron spectra recorded with the two instruments are particularly useful in this regard, allowing us to perform laboratory astrophysics measurements on NSTX.

The measurements also provide new atomic data. For example, the L-shell emission lines of titanium shown in figure 10 have not been seen before in tokamak plasma to the best of our knowledge. Line identifications will become especially important as trace amounts of tungsten are injected into NSTX plasma in the future.

Acknowledgments

This work was performed under the auspices of the US Department of Energy by Lawrence Livermore National Laboratory under contract DE-AC52-07NA27344, and supported in part by the General Plasma Science program of the Office of Fusion Energy Sciences of the Department of Energy. PC and AS were supported by DOE grant DE-FG02-08ER54951.

References

Beiersdorfer P 2003 *Annu. Rev. Astron. Astrophys.* **41** 343
Beiersdorfer P, Bitter M, Roquemore L, Lepson J K and Gu M F 2006 *Rev. Sci. Instrum.* **77** 10F306
Beiersdorfer P, Lepson J K, Bitter M, Hill K W and Roquemore L 2008 *Rev. Sci. Instrum.* **79** 10E318
Beiersdorfer P, Lepson J K, Brown G V, Utter S B, Kahn S M, Liedahl D A and Mauche C W 1999b *Astrophys. J.* **519** L185
Beiersdorfer P, López-Urrutia J R C, Springer P, Utter S B and Wong K L 1999a *Rev. Sci. Instrum.* **70** 276
Beiersdorfer P, Magee E, Träbert E, Chen H, Lepson J K, Gu M F and Schmidt M 2004 *Rev. Sci. Instrum.* **75** 3723
Beiersdorfer P, Scofield J H and Osterheld A L 2003 *Phys. Rev. Lett.* **90** 235003
Beiersdorfer P, von Goeler S, Bitter M, Hinnov E and Bell R 1988 *Phys. Rev. A.* **37** 4153
Chen H, Beiersdorfer P, Heeter L A, Liedahl D A, Naranjo-Rivera K L, Träbert E, Gu M F and Lepson J K 2004 *Astrophys. J.* **611** 598
Chowdhuri M B, Morita S and Goto M 2008a *Appl. Opt.* **47** 135
Chowdhuri M B, Morita S, Goto M and Sasai H 2008b *Rev. Sci. Instrum.* **79** 10F537
Clementson J, Beiersdorfer P and Magee E W 2008 *Rev. Sci. Instrum.* **79** 10F538
Clementson J, Beiersdorfer P, Roquemore L and Skinner C H 2010 *Rev. Sci. Instrum.* (in preparation)
Delgado Aparicio L *et al* 2009 *Nucl. Fusion* **49** 085028
Fonck R J, Ramsey A T and Yelle R V 1982 *Appl. Opt.* **21** 2115
Graf A T *et al* 2008 *Can. J. Phys.* **86** 307
Gu M F 2008 *Can. J. Phys.* **86** 675
Hansen S B 2003 *PhD Thesis* University of Nevada, Reno
Harada T and Kita T 1980 *Appl. Opt.* **19** 3987
Hinnov E, Bol K, Dimock D, Hawryluk R J, Johnson D, Mattioli M, Meservey E and von Goeler S 1978 *Nucl. Fusion* **18** 1305
Kato T *et al* 2008 *J. Phys. B: At. Mol. Opt. Phys.* **41** 035703
Lepson J K and Beiersdorfer P 2005 *Phys. Scr.* T **120** 62
Lepson J K, Beiersdorfer P, Behar E and Kahn S M 2003 *Astrophys. J.* **590** 604
Lepson J K, Beiersdorfer P, Bitter M and Kahn S M 2008 *Can. J. Phys.* **86** 175

Nakano N, Kuroda H, Kita T and Harada T 1984 *Appl. Opt.* **23** 2386
Schwob J L, Wouters A W, Suckewer S and Finkenthal M 1987 *Rev. Sci. Instrum.* **77** 1601
Stratton B C, Bitter M, Hill K W, Hillis D L and Hogan J T 2008 *Fusion Sci. Technol.* **53** 431
Utter S B, Brown G V, Beiersdorfer P, Clothiaux E G and Podder N K 1999 *Rev. Sci. Instrum.* **70** 284
Wilcox P G, Safronova A S, Kantsyrev V L, Safronova U I, Williamson K M, Yilmaz M F, Clementson J, Beiersdorfer P and Struve K W 2008 *Rev. Sci. Instrum.* **79** 10F543